Journal of Materials Chemistry A

ROYAL SOCIETY OF CHEMISTRY

PAPER

View Article Online
View Journal | View Issue

Cite this: J. Mater. Chem. A, 2023, 11, 2246

Highly efficient photocatalytic formic acid decomposition to syngas under visible light using CdS nanorods integrated with crystalline W_2N_3 nanosheets†

Taotao Wang,[ab] Muqing Chen, *[a] Jinbao Wu[b] and Pingwu Du *[bc]

Received 6th December 2022
Accepted 9th January 2023

DOI: 10.1039/d2ta09482g

rsc.li/materials-a

Syngas (H_2/CO) production by photocatalytic formic acid decomposition is a promising method for solar energy conversion. Furthermore, syngas can be used as a fuel in internal combustion engines and can also be converted to other liquid fuels as well as high-value chemicals. In this study, an efficient photocatalytic system was constructed by combining crystalline W_2N_3 nanosheets and CdS nanorods for formic acid decomposition to syngas with an adjustable ratio. Under visible light illumination, the optimal rate of H_2 production is 262 μmol h^{-1} with 207 μmol h^{-1} for CO generation, which are among the highest values achieved from photocatalytic syngas production. Meanwhile, the apparent quantum yields of H_2 and CO evolution are 17.6% and 16.9%, respectively. Further experimental results demonstrate that the heterostructures formed between CdS and W_2N_3 can effectively facilitate interfacial charge transfer and separation. This work also provides insight into developing a novel and low-cost approach for renewable energy conversion.

Introduction

With the rapid development of the economy and the continuous consumption of fossil energy, energy shortages and environmental pollution are becoming increasingly serious.[1–5] Therefore, it is highly significant and challenging to develop renewable energy alternatives.[6–9] Syngas (H_2/CO) is a kind of fuel used in internal combustion engines and is available from coal, natural gas, and biomass.[10–12] Furthermore, it can also be converted to other liquid fuels and high-value chemicals by the Fischer–Tropsch process.[13–15] However, the industrial synthesis process of syngas is complicated. The requirements of high temperature and high pressure result in severe energy consumption.[16] In recent decades, photocatalysis as an efficient solar energy conversion method has been extensively researched, such as photocatalytic CO_2 reduction and photocatalytic formic acid decomposition.[17–22] Nevertheless, syngas production by photocatalytic CO_2 reduction is limited by the low yield and a wide variety of byproducts.[23,24] Formic acid (FA) can be a sustainable source of syngas with low cost, low toxicity, and high gravimetric hydrogen and carbon capacity.[25,26] Formic acid decomposition involves two simultaneous reactions of dehydration and dehydrogenation to produce syngas with byproducts of H_2O and CO_2.[27,28] The byproduct of CO_2 can be hydrogenated to produce formic acid and can also be recycled by other methods to achieve a sustainable cycle of chemical energy.[18,29–31]

Photocatalytic FA decomposition is also an efficient method to produce ratio-tunable syngas, usually using earth-abundant photocatalysts under sunlight irradiation. Therefore, the process is cost-effective and environmentally friendly and is better than thermal or electrocatalytic FA decomposition using precious-metal catalysts.[32–34] As early as 1984, Michio Matsumura reported that syngas and CO_2 could be detected when using platinized CdS powder as a photocatalyst for FA decomposition.[35] Aleksey and coworkers studied the mechanism of formate photodecomposition and reported the coupled catalysis effect of hydrogenase and Cd^0 formed *in situ* on the surface of CdS.[36] Impressively, Shuang Cao and coworkers synthesized ultrasmall CoP nanoparticles and combined them with CdS@RGO, which presented a H_2 production rate of 182 μmol mg^{-1} h^{-1} with excellent long-term stability (>7 days) and selectivity (>99.5%).[37] Other transition metal phosphide-based photocatalysts also show high selectivity for FA dehydrogenation with almost no CO evolution, such as FeP and NiCoP.[19,38]

[a]School of Environment and Civil Engineering, Dongguan University of Technology, Dongguan, Guangdong Province, 523808, P. R. China. E-mail: mqchen@ustc.edu.cn
[b]Hefei National Laboratory for Physical Sciences at Microscale, Anhui Laboratory of Advanced Photon Science and Technology, CAS Key Laboratory of Materials for Energy Conversion, Department of Materials Science and Engineering, University of Science and Technology of China, 96 Jinzhai Road, Hefei, Anhui Province, 230026, P. R. China. E-mail: dupingwu@ustc.edu.cn
[c]National Synchrotron Radiation Laboratory, University of Science and Technology of China, 443 Huangshan Road, Hefei, Anhui Province, 230029, P. R. China

† Electronic supplementary information (ESI) available. See DOI: https://doi.org/10.1039/d2ta09482g

Although numerous photocatalysts have been developed, there are still few excellent photocatalysts for syngas production from FA decomposition. Recently, our group reported that homogeneous Fe-salen can be used as a low-cost and highly efficient catalyst for photocatalytic FA decomposition.[18] A rate of 150 μmol mg^{-1} h^{-1} for H_2 production can be observed with a relatively low rate of 71.5 μmol mg^{-1} h^{-1} for CO evolution by using Fe-salen with CdS nanorods under optimal conditions. Homogeneous catalytic systems for FA decomposition still show inherent separation and recovery problems, which may hinder their practical implementation.[25,39] Therefore, it is significant to develop a low-cost, robust, and durable heterogeneous photocatalyst to produce a large amount of syngas from photocatalytic FA decomposition.

Herein, we report the use of crystalline W_2N_3 nanosheets combined with CdS nanorods to construct a heterogeneous composite for the highly efficient visible light photocatalytic conversion of FA to syngas. W_2N_3 has attracted much attention as an active catalyst for electrocatalytic H_2 evolution due to its Pt-like characteristics.[40,41] Moreover, it is also a good metallic photocatalyst with a high carrier density, excellent conductivity, and an extremely wide light absorption range.[42–45] The crystalline W_2N_3 nanosheets were prepared through a hydrothermal method with subsequent high-temperature calcination in an ammonia atmosphere. Heterostructures between W_2N_3 and CdS were formed after compounding W_2N_3 nanosheets with CdS nanorods and a heat treatment process, which can facilitate interfacial charge transfer and suppress the recombination of photogenerated charges. The hybrid CdS/W_2N_3 photocatalyst demonstrates a remarkable syngas production rate of ~262 μmol h^{-1} for H_2 and ~207 μmol h^{-1} for CO with excellent stability (>50 h) under optimum conditions. These rate values of H_2 and CO generation are 9.4 and 11.5 times higher than those of bare CdS, respectively. In addition, apparent quantum yields of 17.6% and 16.9% for H_2 and CO production can be achieved under 420 nm monochromatic light, which are among the highest values achieved from photocatalytic syngas production.

Results and discussion

Crystalline W_2N_3 nanosheets were prepared by a two-step method. First, a hydrothermal process was used to synthesize WO_3 nanosheets. Then, WO_3 nanosheets were converted to crystalline W_2N_3 nanosheets *via* high-temperature treatment in an ammonia atmosphere. Fig. 1 shows the micromorphologies of the W_2N_3 and CdS/W_2N_3 (5 wt%) samples. The nanosheet structures of W_2N_3 with sizes of 200 to 500 nm can be observed in Fig. 1a and S1b.† The powder mixture was first prepared by mixing CdS nanorods and W_2N_3 nanosheets in ethanol with stirring and ultrasonication. After drying under N_2, the mixture was ground and calcined under argon. Fig. 1b shows that the hybrid CdS/W_2N_3 samples are successfully prepared, and W_2N_3 nanosheets are well dispersed. The CdS nanorods are ~1 μm in length and ~50 nm in diameter (Fig. S1a†). After being ground and calcined, the CdS nanorods show no obvious changes in morphology. Fig. 1c presents some short and disordered nanorods, which can be attributed to the grinding and calcining

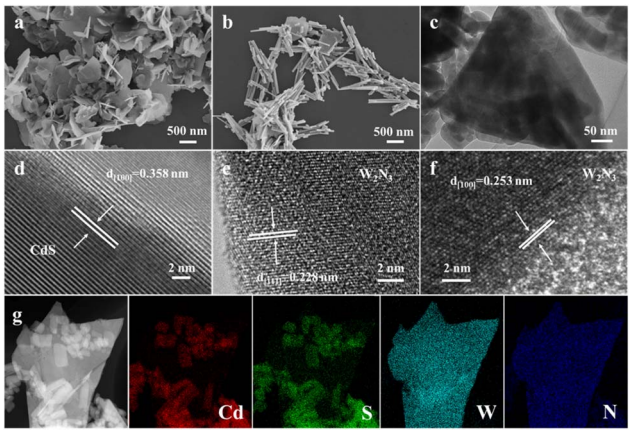

Fig. 1 SEM images of (a) W_2N_3 nanosheets and (b) CdS/W_2N_3 samples (5 wt%). (c) High-resolution TEM image of CdS/W_2N_3 samples (5 wt%). (d–f) High-magnification HRTEM images of CdS/W_2N_3 samples (5 wt%). (g) HAADF-STEM and corresponding EDX mapping images of CdS/W_2N_3 samples (5 wt%).

processes. Good contact between W_2N_3 nanosheets and CdS nanorods can also be observed. The crystalline structures of the hybrid samples were investigated by HRTEM. Fig. 1d exhibits an interplanar crystal spacing of ~0.358 nm, which corresponds to the (100) crystal facet of hexagonal CdS. The interplanar crystal spacings of 0.228 and 0.253 nm can be indexed to the (111) and (100) crystal planes of W_2N_3, respectively (Fig. 1e and f). Energy dispersive X-ray (EDX) elemental mappings are displayed in Fig. 1g, which further confirm the good contact and the formation of the heterojunction between W_2N_3 and CdS.

The composition and crystallinities of CdS/W_2N_3, CdS nanorods, and W_2N_3 nanosheets were determined by X-ray diffraction (XRD). Fig. 2a shows the distinct peaks of CdS nanorods, which are well matched with the hexagonal phase (PDF #65-3414). The diffraction patterns of W_2N_3 nanosheets correspond well with the hexagonal phase according to previous reports.[46–48] No obvious peaks of W_2N_3 can be observed from the patterns of the hybrid CdS/W_2N_3 (5 wt%) sample, which can be ascribed to the relatively low content of W_2N_3. Furthermore, the optical absorption properties of the prepared samples were investigated through ultraviolet-visible diffuse reflectance absorption spectroscopy. Fig. 2b shows the enhanced visible light absorption of the CdS/W_2N_3 sample compared to bare CdS

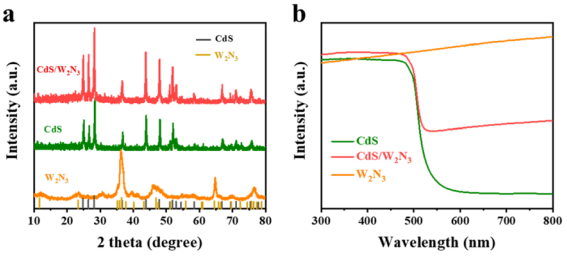

Fig. 2 (a) XRD patterns and (b) diffuse reflectance UV-vis spectra of the samples.

nanorods. However, the absorption edges of CdS/W_2N_3 and CdS are nearly the same, indicating that they have the same bandgap (~2.4 eV, Fig. S2†). Moreover, pure W_2N_3 nanosheets show absorptions in the visible region and demonstrate a band gap of 2.56 eV (Fig. S3†).

The surface chemical composition and valence states of the hybrid CdS/W_2N_3 sample were researched by X-ray photoelectron spectroscopy (XPS). The typical XPS spectra of CdS can be observed in Fig. 3a and b. The Cd 3d spectrum shows two peaks at 404.4 and 411.1 eV, corresponding to Cd $3d_{5/2}$ and Cd $3d_{3/2}$, respectively. For the S 2p spectra, two peaks located at 160.8 and 161.9 eV are assigned to S $2p_{3/2}$ and S $2p_{1/2}$, respectively. The comparison of XPS spectra for CdS and 5 wt% CdS/W_2N_3 can be seen in Fig. S4.† Peaks of Cd $3d_{5/2}$ and Cd $3d_{3/2}$ in CdS/W_2N_3 shift slightly (~0.2 eV) towards high binding energy compared to CdS, suggesting a good contact and interaction between CdS and W_2N_3. Moreover, the high-resolution XPS spectra of W 4f can be fitted into four peaks, two peaks at 32.4 and 34.5 eV corresponding to the W–N bond (Fig. 3c). The other two peaks at 35.3 and 37.4 eV belong to the W–O bond, which can be attributed to the adsorbed oxygen-containing species by W_2N_3 (the main sources are H_2O and O_2 in the air).[49] This indicates that W_2N_3 nanosheets have a strong affinity for O and are necessary for photocatalytic H_2 evolution. The N 1s spectrum is displayed in Fig. 3d with two distinct peaks. The first peak at 397.0 eV corresponds to the W–N bond, and the other peak at 399.1 eV can be ascribed to the N atoms near the N vacancies.[48]

To study the photocatalytic activity of CdS/W_2N_3 for FA decomposition, tests were performed under visible light irradiation (λ > 420 nm) in an FA solution with 2 mg samples. As shown in Fig. 4a, the H_2 evolution performance of CdS nanorods is significantly improved after compounding with different amounts of W_2N_3 nanosheets. The 1 wt% CdS/W_2N_3 sample exhibited an improved H_2 generation rate of 134 μmol h^{-1} at pH 3.5 in 6 M FA solution. The maximum H_2 generation rate of 262 μmol h^{-1} was obtained using the 5 wt% CdS/W_2N_3 sample, which was 9.4 times higher than that of bare CdS (28 μmol h^{-1}). Bare W_2N_3 nanosheets show poor photocatalytic performance

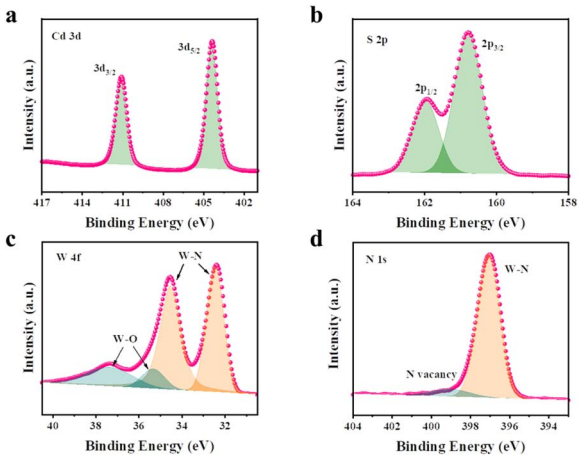

Fig. 3 XPS data of CdS/W_2N_3 samples (5 wt%). High-resolution XPS spectra of (a) Cd 3d, (b) S 2p, (c) W 4f, and (d) N 1s.

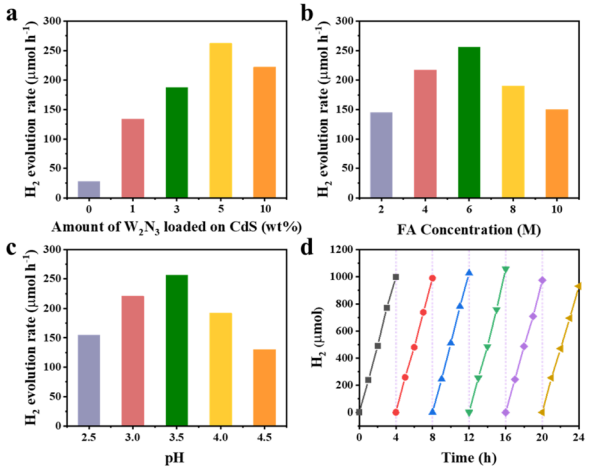

Fig. 4 (a) Visible light photocatalytic performance of H_2 evolution for CdS nanorods composited with different amounts of W_2N_3 nanosheets in 20 mL 6 M formic acid solution at pH 3.5 using a 2 mg sample. (b) Effect of formic acid concentration on the H_2 evolution rate. The photocatalytic system contained 20 mL formic acid solution with 2 mg CdS/W_2N_3 photocatalyst (5 wt%). The pH of the solution was controlled at 3.5 with NaOH. (c) Effect of pH on the H_2 production rate in 20 mL 6 M formic acid solution with 2 mg CdS/W_2N_3 photocatalyst (5 wt%). (d) Photocatalytic H_2 evolution cycling runs in 20 mL 6 M formic acid solution at pH 3.5 with 2 mg CdS/W_2N_3 photocatalyst (5 wt%).

of FA decomposition, and H_2 and CO cannot be detected by chromatography (Fig. 6a). When the content of W_2N_3 nanosheets increased to 10 wt%, the H_2 production rate decreased to 222 μmol h^{-1}. This can be due to the reduced amount of CdS and insufficient photogenerated electrons. In addition, the FA concentration also affects the H_2 evolution rate of photocatalytic FA decomposition (Fig. 4b). The H_2 production rate of the CdS/W_2N_3 sample (5 wt%) in 2 M FA solution with pH 3.5 reached 145 μmol h^{-1}. With the increase in FA concentration, a volcano-shaped curve of the H_2 production rate can be observed, and the optimal concentration is 6 M. An increase in the concentration of formic acid can promote reaction (2) in Fig. 8 with producing more H^+, resulting in an improved H_2 evolution rate. However, excess H^+ can inhibit reaction (3) and lead to a poor oxidation half-reaction and photocatalytic activity. Therefore, when the FA concentration increased to 8 and 10 M, the H_2 evolution rate decreased. Furthermore, the pH of the FA solution also has an effect on the photocatalytic H_2 evolution performance. In Fig. 4c, the 5 wt% CdS/W_2N_3 sample shows a H_2 production rate of 155 μmol h^{-1} at pH 2.5. As the pH increases by adding NaOH, the formed sodium formate can effectively promote the cleavage of the C–H bond and accelerate the reaction process.[50,51] The optimal pH of the reaction solution was 3.5. However, excess undissolved NaOH can affect the light absorption of the photocatalyst, resulting in performance degradation. Cyclic stability tests of the 5 wt% CdS/W_2N_3 sample for H_2 production were carried out in 6 M FA solution at pH 3.5 under visible light irradiation. There was no obvious change in H_2 evolution during the six cycles, suggesting the outstanding stability of the CdS/W_2N_3 photocatalyst for FA

decomposition. The photocatalytic performance with different amount of catalysts were also evaluated in 20 mL formic acid solution (6.0 M) at pH 3.5 to find the optimal amount of catalysts. As shown in Table S1,† 2 mg of the catalysts demonstrate the highest H_2 and CO evolution rates (μmol mg^{-1} h^{-1}), indicating the maximum utilization of light and photocatalysts.

CO evolution rates were also investigated under different conditions. Usually, Cd^{2+} ions can be produced due to the photocorrosion of CdS in FA solution and further reduced to Cd^0 as a catalyst to produce CO.[36] The specific process is that formate species are oxidized by holes to produce $CO_2^{\bullet-}$ anion radicals, which can be reduced with H^+ and e^- to generate CO.[18,19] CO_2 is the product of further oxidation of $CO_2^{\bullet-}$ anion radical by holes. As shown in Fig. 5a, the combination of W_2N_3 nanosheets and CdS nanorods also promotes CO production. This consequence can be due to the facilitated interfacial charge separation and transfer by the heterostructures, leading to the enhancement of photocatalytic activity. The 1 wt% CdS/W_2N_3 sample exhibited a rate of 156 μmol h^{-1} for CO production in 6 M formic acid solution at pH 3.5, which was much higher than that of pure CdS (18 μmol h^{-1}). For CO evolution, the optimal loading amount of W_2N_3 is 3 wt% with a CO evolution rate of 287 μmol h^{-1} instead of 5 wt% for H_2 evolution. With a further increase in the W_2N_3 content, many photogenerated electrons are transferred to W_2N_3, leading to less reduced Cd^0 and a decreased CO evolution rate. Fig. 5b shows the CO evolution rates of the 5 wt% CdS/W_2N_3 sample in the FA solution with different concentrations. The same regularity as the H_2 production rate can be observed. The pH effects on CO generation were investigated in 6 M formic acid using the 5 wt% CdS/W_2N_3 samples. At pH 2.5, the CO evolution rate of 65 μmol h^{-1} is much smaller than the H_2 production rate of 156 μmol h^{-1}. This result can be ascribed to the inhibition of reaction (3) under acidic conditions, resulting in less $CO_2^{\bullet-}$ and CO production. Moreover, the optimal pH is also 3.5 with a CO production rate of 207 μmol h^{-1}, which is 11.5 times higher than that of pure CdS (18 μmol h^{-1}). Similarly, the 5 wt% CdS/W_2N_3 sample exhibited excellent cyclic stability during the six cycles in 6 M formic acid solution (Fig. 5d).

Fig. 6a shows the photocatalytic activity comparison of different samples in 6 M FA solution at pH 3.5. The CdS–W_2N_3 sample was synthesized by simply mixing CdS nanorods with W_2N_3 nanosheets and showed much lower H_2 and CO evolution rates than CdS/W_2N_3. This further indicates better contact and the formation of heterostructures between CdS and W_2N_3. To explore the long-term stability of the CdS/W_2N_3 sample for photocatalytic FA decomposition, experiments were performed under visible light irradiation ($\lambda > 420$ nm) in 6 M FA solution at pH 3.5. The H_2 and CO evolution present excellent stabilities during 54 h of continuous testing (Fig. 6b). The total amounts of H_2 and CO are 6.75 and 6.05 mmol, respectively. In comparison, Fig. S5† exhibits the H_2 and CO evolution of pure CdS nanorods for 12 h. The significantly enhanced stability of CdS/W_2N_3 can be ascribed to the rapid surface charge transfer as well as the suppressed charge recombination. In addition, W_2N_3 loading increases the active sites of the reaction and promotes the reaction kinetics. The fast consumption of photoelectrons and holes also effectively inhibits photocorrosion. Fig. S6† shows the TEM images for CdS/W_2N_3 after 54 h of the stability test. The corresponding XPS spectra of CdS/W_2N_3 after the stability test are also shown in Fig. S7.† The peak intensity in the N 1s spectrum is obviously decreased after the stability test, which can be due to the partial oxidation of W_2N_3 during the reaction.

Furthermore, the apparent quantum yields (AQYs) of H_2 and CO production were measured in 6.0 M formic acid solution at pH 3.5 using a 2 mg CdS/W_2N_3 sample (5 wt%) under 420 nm

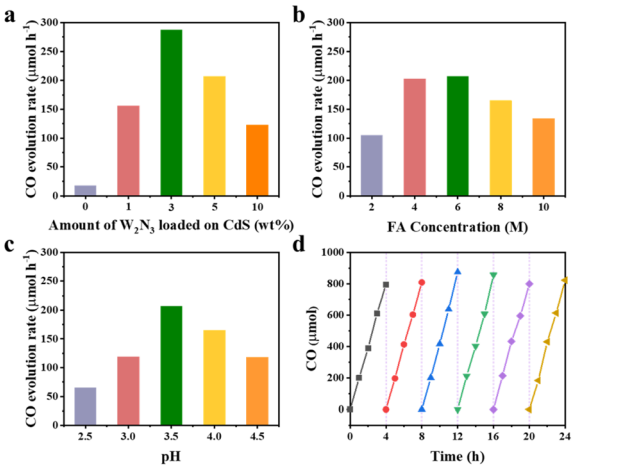

Fig. 5 (a) Visible light photocatalytic performance of CO evolution for CdS nanorods composited with different amounts of W_2N_3 nanosheets. (b) Effect of formic acid concentration on CO production rate. (c) Effect of pH on the CO production rate. (d) Cycling runs for photocatalytic CO production. The specific reaction conditions can be seen in the legend of Fig. 4.

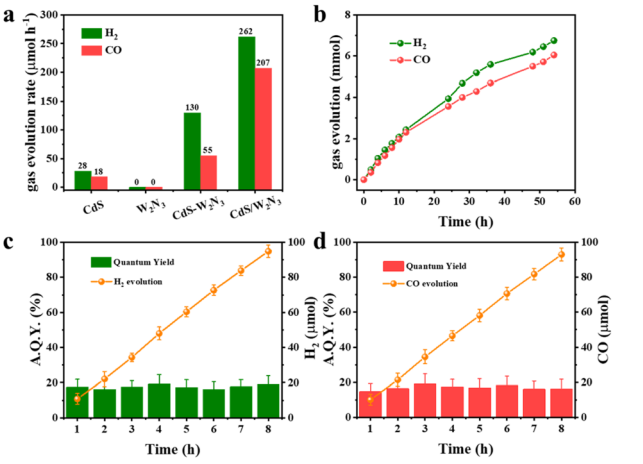

Fig. 6 (a) Photocatalytic performance of CdS nanorods, W_2N_3 nanosheets, CdS–W_2N_3 (5 wt%), and CdS/W_2N_3 (5 wt%) for H_2 and CO evolution in 20 mL 6 M FA aqueous solution at pH 3.5 with 2 mg sample. (b) Long-term evolution of H_2 and CO under 420 nm light irradiation using 2 mg CdS/W_2N_3 photocatalyst (5 wt%) in 20 mL 6 M FA aqueous solution at pH 3.5. The time courses of (c) H_2 and (d) CO evolution and apparent quantum yields under 420 nm monochromatic light irradiation using CdS/W_2N_3 photocatalyst (5 wt%). The photocatalytic solution was 20 mL 6 M FA aqueous solution at pH 3.5.

light irradiation. As shown in Fig. 6c, the highest AQY for H_2 production reached 19.2% after 4 h of irradiation. During 8 h of irradiation, the average AQY for H_2 evolution reached 17.6%. For CO evolution, the average AQY reached 16.9% during 8 h irradiation (Fig. 6d). These results indicate the effective solar energy conversion in this photocatalytic system and the huge potential of the CdS/W_2N_3 photocatalyst for highly efficient syngas production from photocatalytic FA conversion. Table S2† exhibits the comparison of the H_2 and CO generation rate for photocatalytic formic acid decomposition of the CdS/W_2N_3 with other reported high performance photocatalysts.

To study the effect of W_2N_3 on photogenerated charge migration and separation, photoelectrochemical and photoluminescence tests were carried out. The photocurrent response tests were performed using a three-electrode system in 0.5 M Na_2SO_4. As shown in Fig. 7a, a remarkable increase in the photocurrent of the CdS/W_2N_3 sample can be observed compared to that of pure CdS. Electrochemical impedance spectroscopy (EIS) measurements were conducted under illumination. The electron transfer resistance is reflected by the semicircle diameter of the Nyquist plots in Fig. 7b. A markedly decreased charge transfer resistance can be seen after W_2N_3 loading, which suggests an accelerated charge transfer process. Furthermore, the process of electron transfer was also investigated by photoluminescence (PL) with a 405 nm excitation wavelength. For pure CdS nanorods, an intense peak due to the near-band-edge emission and a broad peak caused by the surface defects are displayed in Fig. 7c. The CdS/W_2N_3 sample shows a much weaker peak intensity than pure CdS nanorods, which illustrates a prominent reduction in charge recombination. These results all indicate that the heterojunction promotes the transport of photogenerated charges between CdS and W_2N_3, which also ensures the efficient separation and utilization of photogenerated electrons and holes, thereby further enhancing the photocatalytic activity. Mott–Schottky (MS) measurements were carried out to identify the electronic band positions of CdS and W_2N_3 (Fig. S8†). The conduction bands of CdS and W_2N_3 are −0.73 eV and −0.71 eV *vs.* NHE, respectively. Considering the band gaps of CdS and W_2N_3, their valence bands can be 1.67 eV and 1.85 eV *vs.* NHE, respectively. The formed type-II heterojunction also explains the direction of electron transfer, which can be seen in Fig. 7d.

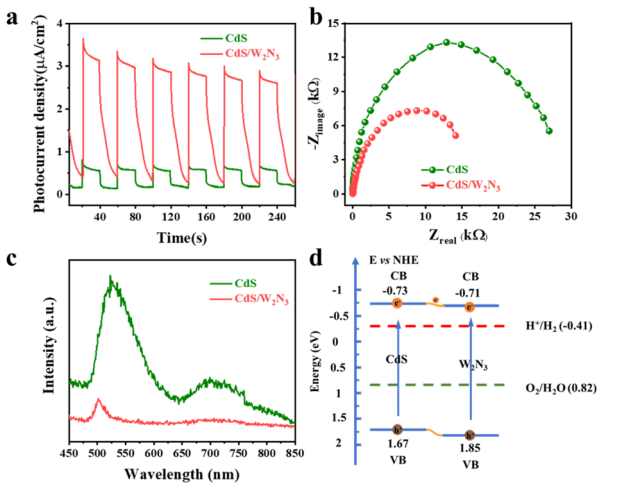

Fig. 7 (a) Photocurrent responses, (b) EIS spectra under illumination, (c) photoluminescence spectra, and (d) band structures of CdS and W_2N_3.

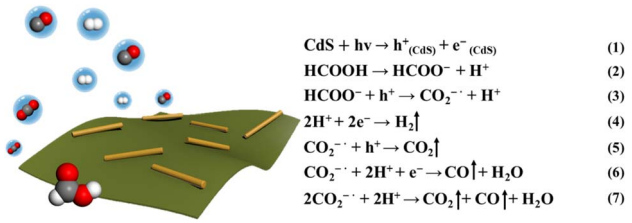

Fig. 8 Proposed mechanism for photocatalytic FA decomposition.

Conclusions

In summary, we successfully synthesized ultrathin crystalline W_2N_3 nanosheets, composited them with CdS nanorods, and introduced this catalyst to the photocatalytic conversion of formic acid to syngas. Notably, this hybrid photocatalyst exhibited a prominent syngas production rate and excellent apparent quantum yields with superior long-term stability. The excellent photocatalytic performance can be mainly attributed to the facilitated charge transfer and separation caused by the formed type-II heterojunction. The composited W_2N_3 nanosheets also increase the number of active sites and accelerate the reaction kinetics. Furthermore, photocatalytic formic acid decomposition shows great application prospects in solar energy conversion. This work also provides new ideas for photocatalyst design and syngas production.

Conflicts of interest

There are no conflicts to declare.

Acknowledgements

This work was financially supported by National Natural Science Foundation of China (22225108, 21971229, 52172053, U1932214), Hefei National Laboratory for Physical Sciences at Microscale, and National Synchrotron Radiation Laboratory at USTC.

Notes and references

1 Y. He, T. Hamann and D. Wang, *Chem. Soc. Rev.*, 2019, **48**, 2182–2215.
2 S. C. Warren and E. Thimsen, *Energy Environ. Sci.*, 2012, **5**, 5133–5146.
3 K. Maeda, K. Teramura, D. Lu, T. Takata, N. Saito, Y. Inoue and K. Domen, *Nature*, 2006, **440**, 295.
4 K. Sivula and R. Van De Krol, *Nat. Rev. Mater.*, 2016, **1**, 1–16.

5 T. Hisatomi, J. Kubota and K. Domen, *Chem. Soc. Rev.*, 2014, **43**, 7520–7535.
6 K. Barnham, M. Mazzer and B. Clive, *Nat. Mater.*, 2006, **5**, 161–164.
7 K. H. Ng, S. Y. Lai, C. K. Cheng, Y. W. Cheng and C. C. Chong, *Chem. Eng. J.*, 2021, **417**, 128847.
8 M.-Y. Qi, M. Conte, M. Anpo, Z.-R. Tang and Y.-J. Xu, *Chem. Rev.*, 2021, **121**, 13051–13085.
9 L. Yuan, C. Han, M.-Q. Yang and Y.-J. Xu, *Int. Rev. Phys. Chem.*, 2016, **35**, 1–36.
10 J. R. Rostrup-Nielsen, *Catal. Today*, 2002, **71**, 243–247.
11 J. R. Rostrup-Nielsen, *Catal. Today*, 2000, **63**, 159–164.
12 J. Daniell, M. Köpke and S. D. Simpson, *Energies*, 2012, **5**, 5372–5417.
13 R. G. dos Santos and A. C. Alencar, *Int. J. Hydrogen Energy*, 2020, **45**, 18114–18132.
14 X. Pan, F. Jiao, D. Miao and X. Bao, *Chem. Rev.*, 2021, **121**, 6588–6609.
15 Z. X. Wang, T. Dong, L. X. Yuan, T. Kan, X. F. Zhu, Y. Torimoto, M. Sadakata and Q. X. Li, *Energy Fuels*, 2007, **21**, 2421–2432.
16 S. Cui, C. Yu, X. Tan, H. Huang, X. Yao and J. Qiu, *ACS Sustainable Chem. Eng.*, 2020, **8**, 3328–3335.
17 X. Li, Y. Sun, J. Xu, Y. Shao, J. Wu, X. Xu, Y. Pan, H. Ju, J. Zhu and Y. Xie, *Nat. Energy*, 2019, **4**, 690–699.
18 R. M. Irfan, T. Wang, D. Jiang, Q. Yue, L. Zhang, H. Cao, Y. Pan and P. Du, *Angew. Chem.*, 2020, **59**, 14818–14824.
19 T. Wang, L. Yang, D. Jiang, H. Cao, A. C. Minja and P. Du, *ACS Appl. Mater. Interfaces*, 2021, **13**, 23751–23759.
20 C. Ning, Z. Wang, S. Bai, L. Tan, H. Dong, Y. Xu, X. Hao, T. Shen, J. Zhao and P. Zhao, *Chem. Eng. J.*, 2021, **412**, 128362.
21 B. Han, S. Liu, N. Zhang, Y.-J. Xu and Z.-R. Tang, *Appl. Catal., B*, 2017, **202**, 298–304.
22 Z.-R. Tang, B. Han, C. Han and Y.-J. Xu, *J. Mater. Chem. A*, 2017, **5**, 2387–2410.
23 X. Li, J. Yu, M. Jaroniec and X. Chen, *Chem. Rev.*, 2019, **119**, 3962–4179.
24 R. Li, W. Zhang and K. Zhou, *Adv. Mater.*, 2018, **30**, 1705512.
25 M. Grasemann and G. Laurenczy, *Energy Environ. Sci.*, 2012, **5**, 8171–8181.
26 C. Rice, S. Ha, R. Masel, P. Waszczuk, A. Wieckowski and T. Barnard, *J. Power Sources*, 2002, **111**, 83–89.
27 M. F. Kuehnel, D. W. Wakerley, K. L. Orchard and E. Reisner, *Angew. Chem.*, 2015, **54**, 9627–9631.
28 J. A. Nasir, M. Hafeez, M. Arshad, N. Z. Ali, I. F. Teixeira, I. McPherson and M. A. Khan, *ChemSusChem*, 2018, **11**, 2587–2592.
29 Y. Y. Cai, X. H. Li, Y. N. Zhang, X. Wei, K. X. Wang and J. S. Chen, *Angew. Chem.*, 2013, **125**, 12038–12041.
30 X. Wang, Q. Meng, L. Gao, Z. Jin, J. Ge, C. Liu and W. Xing, *Int. J. Hydrogen Energy*, 2018, **43**, 7055–7071.
31 F.-K. Shang, Y.-H. Li, M.-Y. Qi, Z.-R. Tang and Y.-J. Xu, *Catal. Today*, 2023, **410**, 85–101.
32 B.-S. Choi, J. Song, M. Song, B. S. Goo, Y. W. Lee, Y. Kim, H. Yang and S. W. Han, *ACS Catal.*, 2018, **9**, 819–826.
33 L. Zhang, S. I. Choi, J. Tao, H. C. Peng, S. Xie, Y. Zhu, Z. Xie and Y. Xia, *Adv. Funct. Mater.*, 2014, **24**, 7520–7529.
34 Z. L. Wang, J. M. Yan, Y. Ping, H. L. Wang, W. T. Zheng and Q. Jiang, *Angew. Chem.*, 2013, **125**, 4502–4505.
35 M. Matsumura, M. Hiramoto, T. Iehara and H. Tsubomura, *J. Phys. Chem.*, 1984, **88**, 248–250.
36 A. I. Nedoluzhko, I. A. Shumilin and V. V. Nikandrov, *J. Phys. Chem.*, 1996, **100**, 17544–17550.
37 S. Cao, Y. Chen, H. Wang, J. Chen, X. Shi, H. Li, P. Cheng, X. Liu, M. Liu and L. Piao, *Joule*, 2018, **2**, 549–557.
38 H. Cao, T. Wang, A. C. Minja, D. Jiang and P. Du, *Int. J. Hydrogen Energy*, 2021, **46**, 32435–32444.
39 A. Boddien, B. Loges, F. Gärtner, C. Torborg, K. Fumino, H. Junge, R. Ludwig and M. Beller, *J. Am. Chem. Soc.*, 2010, **132**, 8924–8934.
40 G. Li, J. Song, G. Pan and X. Gao, *Energy Environ. Sci.*, 2011, **4**, 1680–1683.
41 C. Lv, X. Wang, L. Gao, A. Wang, S. Wang, R. Wang, X. Ning, Y. Li, D. W. Boukhvalov and Z. Huang, *ACS Catal.*, 2020, **10**, 13323–13333.
42 W. Huang, Y. Gao, J. Wang, P. Ding, M. Yan, F. Wu, J. Liu, D. Liu, C. Guo and B. Yang, *Small*, 2020, **16**, 2004557.
43 Y. L. Wang, T. Nie, Y. H. Li, X. L. Wang, L. R. Zheng, A. P. Chen, X. Q. Gong and H. G. Yang, *Angew. Chem.*, 2017, **129**, 7538–7542.
44 D. Liu, Y. Xu, M. Sun, Y. Huang, Y. Yu and B. Zhang, *J. Mater. Chem. A*, 2020, **8**, 1077–1083.
45 S. Xu, S. Gong, H. Jiang, P. Shi, J. Fan, Q. Xu and Y. Min, *Appl. Catal., B*, 2020, **267**, 118661.
46 H. Yu, X. Yang, X. Xiao, M. Chen, Q. Zhang, L. Huang, J. Wu, T. Li, S. Chen and L. Song, *Adv. Mater.*, 2018, **30**, 1805655.
47 S. Wang, X. Yu, Z. Lin, R. Zhang, D. He, J. Qin, J. Zhu, J. Han, L. Wang and H.-k. Mao, *Chem. Mater.*, 2012, **24**, 3023–3028.
48 S. Tan, B. M. Tackett, Q. He, J. H. Lee, J. G. Chen and S. S. Wong, *Nano Res.*, 2020, **13**, 1434–1443.
49 J. Hao, H. He, S. Gong, J. Fan, Q. Xu and Y. Min, *ACS Appl. Mater. Interfaces*, 2021, **13**, 19884–19893.
50 H.-F. Wang and Z.-P. Liu, *J. Phys. Chem. C*, 2009, **113**, 17502–17508.
51 B. Peng, H.-F. Wang, Z.-P. Liu and W.-B. Cai, *J. Phys. Chem. C*, 2010, **114**, 3102–3107.